

A Pressure Induced Structural Dichotomy in Isostructural Bis-1,2,3-thiaselenazoly Radical Dimers

Kristina Legin,[†] Alicea A. Leitch,[†] John S. Tse,[‡] Xuezhao Bao,[§] Richard A. Secco,[§] Serge Desgreniers,^{||} Yasuo Ohishi,[⊥] and Richard T. Oakley^{*,†}

[†]Department of Physics and Engineering Physics, University of Saskatchewan, Saskatoon, Saskatchewan S7N 5E2, Canada

[‡]Department of Chemistry, University of Waterloo, Waterloo, Ontario N2L 3G1, Canada

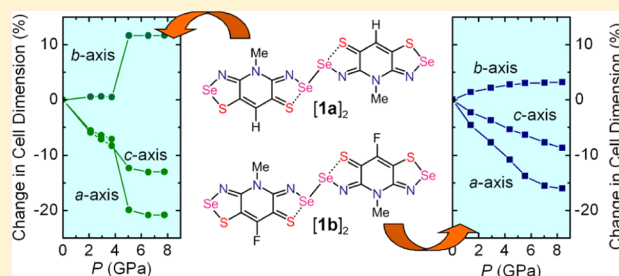
[§]Department of Earth Sciences, University of Western Ontario, London, Ontario N6A 5B7, Canada

^{||}University of Ottawa, Ottawa, Ontario K1N 6N5, Canada

[⊥]Materials Science Division, Japan Synchrotron Radiation Research Institute (JASRI), Spring-8, Sayo, Hyogo 679-5198, Japan

Supporting Information

ABSTRACT: The pressure dependence of the crystal and molecular structure of the bis-1,2,3-thiaselenazoly radical dimer **[1b]₂** has been investigated over the range 0–11 GPa by powder diffraction methods using synchrotron radiation and diamond anvil cell techniques. At ambient pressure, the dimer consists of a pair of radicals linked by a hypervalent 4-center 6-electron S---Se---Se---S σ -bond in an essentially coplanar arrangement. The dimers are packed in cross-braced slipped π -stack arrays running along the x -direction of the monoclinic (space group $P2_1/c$) unit cell. Pressurization to 11 GPa causes the unit cell dimensions a and c to undergo a slow but uniform compression, while the b -axis is slightly elongated. There is virtually no change in the molecular structure or in the slipped π -stack crystal architecture. This behavior is in marked contrast to that of the isostructural radical dimer **[1a]₂**, where the basal fluorine is replaced by hydrogen. Pressurization of this latter material induces a phase change near 4–5 GPa, characterized by a sharp contraction in a and c , and a correspondingly large increase in b . At the molecular level, the transition is associated with a buckling of the σ -bonded dimer to a more conventional π -bonded arrangement. Geometry optimized DFT band structure calculations on **[1b]₂** replicate the observed structural changes and indicate that compression widens both the valence and conduction bands but does not induce band gap closure until >13 GPa. This result is consistent with the measured thermal activation energy for conduction E_{act} which indicates that a metallic state requires pressures > 10 GPa.



INTRODUCTION

The application of physical pressure to crystalline solids can have a profound impact on their structure and electronic properties.¹ While significant changes to ionic materials may require pressures in excess of 200 GPa, molecular elemental solids, notably the heavier chalcogens and halogens, can respond quite dramatically to relatively low pressures (20–30 GPa). Generally, however, the structural transformations involve bond cleavage. For example, the metallization of molecular iodine² is associated with several phase transitions, with complete separation of the atoms occurring near 30 GPa.³ Bond dissociation also occurs for elemental sulfur under pressure,⁴ leading to opening of the S_8 rings of the orthorhombic phase and formation of a helical chain (trigonal) structure which, in turn, recycles to a rhombohedral structure based on S_6 rings.⁵ Analogous trigonal⁶ and rhombohedral⁷ phases are known for selenium.

In light of these findings, reports of pressure-induced changes in the electronic properties of closed shell molecular compounds, particularly those containing heavier chalcogens and halogens, require careful scrutiny. While it is appealing to

explain conductivity enhancements in terms of a broadening of the valence and conduction bands and consequent closure of the associated band gap, the effect may in fact be caused by a structural decomposition. For example, the pressure induced metallization of iodine-substituted aromatics such as *p*-diiodobenzene,⁸ hexaiodobenzene,⁹ and iodonil,¹⁰ which require pressures in excess of 30 GPa, has been suggested to arise from bond dissociation to afford domains of metallic iodine.^{11,12} Enhancement of the conductivity of sulfur,¹³ selenium,¹⁴ and tellurium-based¹⁵ polyacenes has also been observed, with metal-like behavior emerging near or above 20 GPa. However, for these chalcogen-based compounds, crystallographic studies have established that the molecular framework remains intact under compression, and density functional theory (DFT) calculations have confirmed that metallization can be attributed in large part to closure of the electronic band gap.¹⁶

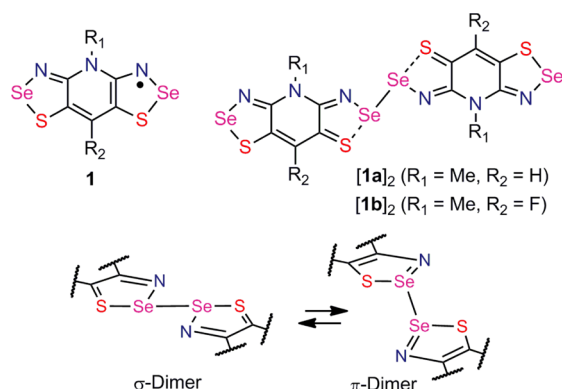
Received: July 6, 2012

Revised: August 14, 2012

Published: August 23, 2012

In comparison to the above materials, the response of the conductivity of the bis-1,2,3-thiaselenazoly radical dimer $[1a]_2$ ($R_1 = \text{Me}$, $R_2 = \text{H}$) (Chart 1) to pressure is quite dramatic.

Chart 1



When isolated in 2005,¹⁷ this compound represented the first example of a heterocyclic selenazyl radical to associate in the solid state through a hypervalent 4-center 6-electron (4c–6e) σ -bond.¹⁸ While dimerization of selenazyl radicals is ubiquitous, association usually takes place via π – π interactions.^{19,20} The radical spins in $[1a]_2$ were nonetheless quenched, and the resulting closed shell molecule displayed transport properties expected for a small band gap semiconductor, with a room temperature conductivity $\sigma(300\text{ K})$ near 10^{-6} S cm^{-1} . However, with relatively mild compression (to 5 GPa), the value of $\sigma(300\text{ K})$ surged upward by 5–6 orders of magnitude, and concomitantly the thermal activation energy E_{act} dropped to near zero.

To understand the origin of the response of $[1a]_2$ to pressure, we carried out a detailed investigation of its crystal structure over the pressure range 0–11 GPa, using synchrotron radiation and diamond anvil cell techniques.²¹ This work confirmed that the metallization did not occur by decomposition, for example, by extrusion of elemental selenium,²² and showed that the application of pressure caused the linear S...Se–Se...S arrangement of the σ -dimer to buckle into a motif best described as a highly distorted π -dimer (Chart 1). While the conversion of a σ -dimer to a π -dimer was, in itself, a novel finding, what made the process remarkable was the fact that the σ - to π -dimer turnover caused a sharp reduction in the HOMO–LUMO gap. As a result, the broadening of the valence and conduction bands occasioned by compression was sufficient to induce closure of the band gap, affording a nominally metallic state. In essence, metallization appeared to arise as much from changes in molecular structure as in solid state packing.

A potential corollary to this interpretation is that, in the absence of molecular buckling, sudden band gap closure and metallization should not be observed. To test this possibility, however, structurally related systems need to be examined. In this regard, we have reported a number of analogues of $[1a]_2$, including the isostructural dimer $[1b]_2$ ($R_1 = \text{Me}$, $R_2 = \text{F}$).²³ The conductivity of this latter material also increases sharply with pressure, like that of $[1a]_2$, and our initial thought was that a similar structural rearrangement (Chart 1) might be at play. To clarify the structural and electronic changes occasioned by compression of $[1b]_2$, we therefore carried out a study of the crystal and molecular structure of $[1b]_2$ as a function of

pressure, again using synchrotron radiation and diamond anvil techniques. To our surprise, we have found that the structural responses of $[1a]_2$ and $[1b]_2$ are quite different; the molecular buckling observed for $[1a]_2$ does *not* occur for $[1b]_2$. Instead the slipped π -stacks are compressed without significant change in the molecular structure of the dimer itself. As in the case of $[1a]_2$, density functional theory (DFT) calculations have been used to replicate the pressure induced changes for $[1b]_2$ and to predict the electronic band gap as a function of pressure. The results indicate a gradual decrease of the band gap with increasing pressure, with full closure not anticipated until well above 13 GPa.

RESULTS

Crystallography. High pressure diffraction data on $[1b]_2$ were collected at room temperature as a function of increasing pressure using synchrotron radiation ($\lambda = 0.51446\text{ \AA}$) and a diamond anvil cell with helium as the pressure transmitting medium. A total of nine data sets from 0 to 11.2 GPa were indexed using DICVOL, as supplied with DASH, and six of these²⁴ were solved starting from a molecular model based on the ambient pressure crystal of $[1b]_2$ with the basal proton replaced by a fluorine atom. During the initial Rietveld refinement, performed using DASH, a rigid-body constraint was maintained, but for the high pressure structures, the sulfur and selenium positions were later released to optimize within the plane of the molecule. A final refinement, using fixed atomic positions and isotropic thermal parameters, was performed using GSAS on three data sets. Unit cell and refinement parameters for these are listed in Table 1, while summaries of

Table 1. Crystal Data for $[1b]_2$

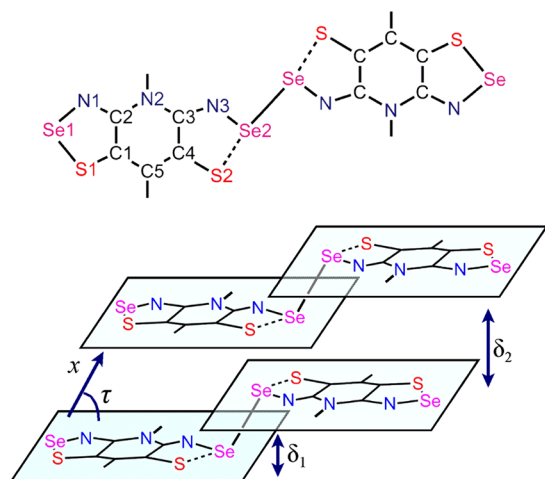
	$\text{C}_6\text{H}_3\text{FN}_3\text{S}_2\text{Se}_2$	$\text{C}_6\text{H}_3\text{FN}_3\text{S}_2\text{Se}_2$	$\text{C}_6\text{H}_3\text{FN}_3\text{S}_2\text{Se}_2$
fw	358.15	358.15	358.15
<i>P</i> , GPa	0.0	4.38	8.40
<i>a</i> , Å	4.28423(11)	3.82021(12)	3.59910(17)
<i>b</i> , Å	13.4658(4)	13.82056(34)	13.88062(35)
<i>c</i> , Å	15.8983(17)	15.0366(14)	14.5372(15)
β , deg	79.300(4)	82.973(6)	84.851(6)
<i>V</i> , Å ³	901.24(9)	787.93(7)	723.31(7)
space group	$P2_1/c$	$P2_1/c$	$P2_1/c$
<i>Z</i>	4	4	4
temp, K	293(2)	293(2)	293(2)
λ , Å	0.51446	0.51446	0.51446
soln method	powder data	powder data	powder data
R_p , R_{wp}	0.0086, 0.0130	0.0100, 0.0142	0.0117, 0.0169

pertinent inter- and intramolecular distances as a function of pressure are presented in Table 2. Figure 1 provides the atom numbering scheme and also defines important intermolecular distances and angles. Representative powder patterns (observed and calculated) are shown in Figure 2.

At ambient pressure, crystals of $[1a]_2$ and $[1b]_2$ both belong to the monoclinic space group $P2_1/c$ and are isostructural. At the molecular level, the radicals are dimerized in a nearly coplanar arrangement, as witnessed by the small interplanar separation δ_1 (Figure 1). The two radicals are linked by a 4c–6e S...Se–Se...S interaction, which leads to a lengthening of the Se2–S2 bond to a value intermediate between the sum of the covalent radii²⁵ and the expected van der Waals contact,²⁶ in keeping with a hypervalent description. At the same time, the N1–C2, N3–C3, and C4–S2 bonds contract in a manner

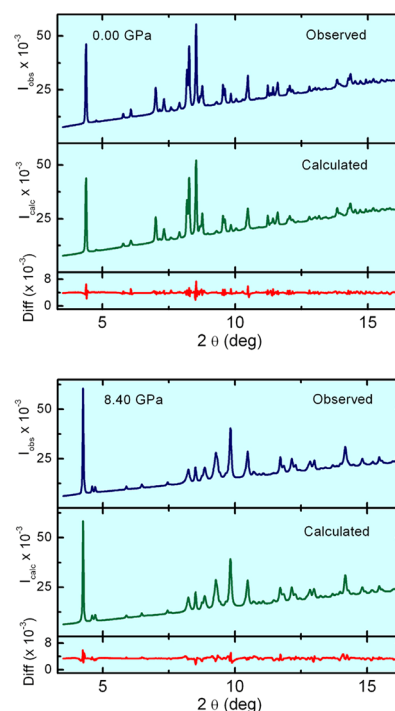
Table 2. Selected Distances^a and Angles^b in [1a]₂ and [1b]₂ as a Function of Pressure

	[1a] ₂			[1b] ₂		
press., GPa	0 ^c	5.09 ^d	9.37 ^d	0	4.38	8.40
Se2–Se2'	2.460(2)	2.724	2.669	2.497	2.486	2.557
Se2...S2	2.785(3)	2.252	2.190	2.785	2.808	2.755
S2–C4	1.694(6)	1.767	1.808	1.694	1.759	1.772
δ ₁	0.384	1.578	1.655	0.367	0.335	0.398
δ ₂	3.540	3.119	2.997	3.469	3.182	3.036
τ	46.0	52.3	53.3	35.9	33.6	32.5
Se2...S1', d ₁	3.663	3.077	2.890	3.667	3.485	3.211
S2...Se1', d ₂	3.824	3.856	3.589	4.145	3.795	3.567
Se2...S1', d ₃	4.848	3.579	3.444	3.909	3.666	3.369
S2...Se1', d ₄	3.177	2.843	2.723	3.166	3.064	2.896

^aDistances in Å. ^bAngles in degrees. ^cFrom ref 17a. ^dFrom ref 21.**Figure 1.** Atom numbering scheme and intermolecular structural parameters.

which is consistent with the valence bond formulation shown in Chart 1.²⁷ As illustrated in Figure 3, there are two centrosymmetric dimers per unit cell, each bridged by a single Se2–Se2' bond and packed in cross-braced slipped π -stacks that run parallel to the *a* axis. While the stacking of the dimers is very similar for the two compounds, there is a noticeable difference in the inclination of the slipped π -stacks with respect to the stacking direction, defined in terms of the angle τ (Figure 1). The steeper “tilt” observed for [1a]₂, which leads to a larger unit cell parameter *a* and a correspondingly shorter value of *b*, represents the key to understanding the contrasting pressure dependence of the two compounds.

With the initial application of pressure (< 4 GPa), both structures display a similar response. As may be seen in Figures 4 and 5, which illustrate the absolute and relative changes in cell parameters as a function of pressure, the *a* and *c* axes contract slightly, while the *b* axis becomes marginally longer. The value of δ_2 , the plate-to-plate separation along the π -stacks, decreases slightly, as would be expected, and the inclination of the π -stacks, measured in terms of the tilt angle τ , also increases marginally, so that the molecular plates become more nearly superimposed. The dimer itself also remains much the same as at ambient pressure. The interannular Se2–Se2' σ -bond, the hypervalent Se2...S2 σ -bonds, and the C4–S2 bonds show small but unexceptional variations. Likewise, the value of δ_1 , the interplanar separation of the two halves of the dimer, also

**Figure 2.** Representative powder X-ray diffraction patterns (observed and calculated) for [1b]₂ ($\lambda = 0.51446$ Å) at 0 GPa (above) and 8.40 GPa (below).

remains essentially constant. As reported earlier, [1a]₂ undergoes a phase change between 3.74 and 5.09 GPa, and the divergence in the cell parameters noted above becomes far more pronounced; the values of *a* and *c* drop rapidly, to differing degrees, while *b* rises sharply. Collectively, these unit cell changes translate into a concertina-like compression of the cross-braced π -stack framework (Figure 6). The plate-to-plate separation δ_2 decreases significantly, as would be expected, but in addition, individual ribbons appear to buckle under pressure, as a result of which the planes of the two halves of the dimers separate, and δ_1 increases sharply. At the molecular level, the diselenide bond Se2–Se2' that binds the dimers actually lengthens, the hypervalent Se2...S2 interactions revert to values more in keeping with a covalent Se–S bond, and the C4–S2 bonds lengthen, suggesting that they should no longer be described as terminal thiones. Between 5.09 and 9.37 GPa, the cell changes become more gradual, and all packing and molecular adjustments are, by comparison, minor.

The “pancake” collapse observed for the unit cell of [1a]₂ near 4 GPa is not found for [1b]₂. Instead, the slow but steady divergence in cell parameters seen at pressures below 4 GPa continues, with *a* and *c* decreasing and *b* increasing (slightly) out to 11 GPa, the limit of the measurements. As expected, the plate-to-plate separation δ_2 decreases as the π -stacks are compressed. However, throughout this process, there is no significant change in the structure of the dimer itself; there is no evidence of buckling. Instead, the two halves of the dimer remain nearly coplanar, as indicated by the small value of δ_1 , and the intradimer Se2–Se2' and hypervalent Se2...S2 bonds remain unchanged. For both structures, compression of the lattice produces many close intermolecular contacts. In [1a]₂, these contacts change somewhat abruptly through the phase transition, while in [1b]₂ the contraction is more uniform and gradual (Figure 7). The sheer number of these contacts,

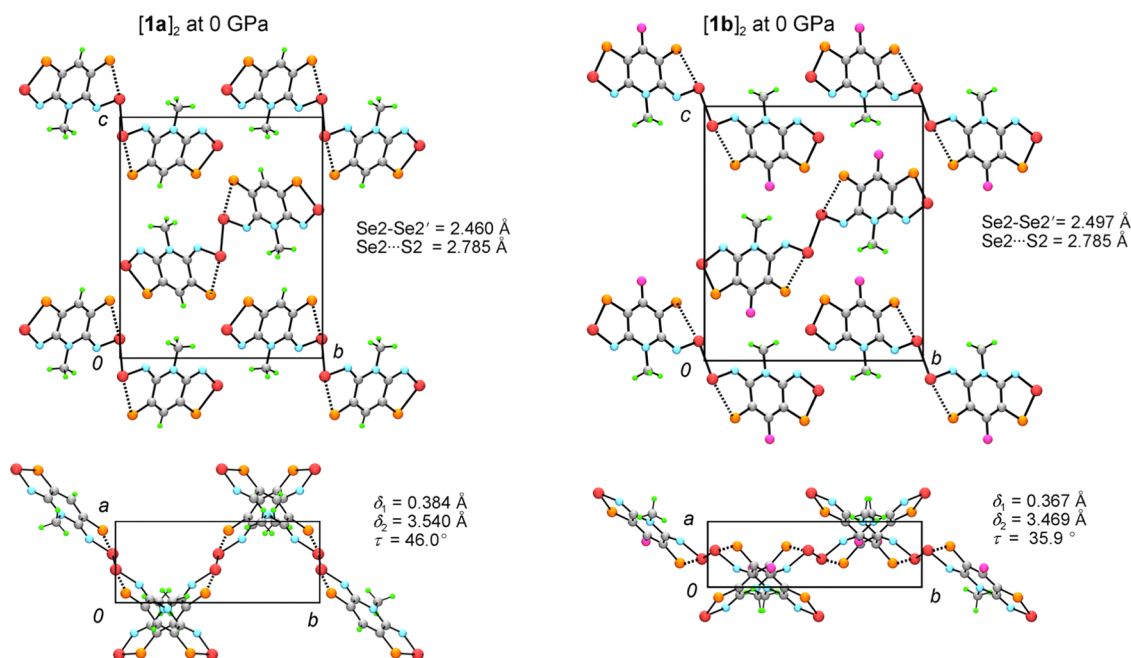


Figure 3. Unit cell drawings of [1a]₂ (left) and [1b]₂ (right) at 0 GPa, viewed along the *a* (above) and *c* (below) axes. See Figure 1 for definition of distances and angles.

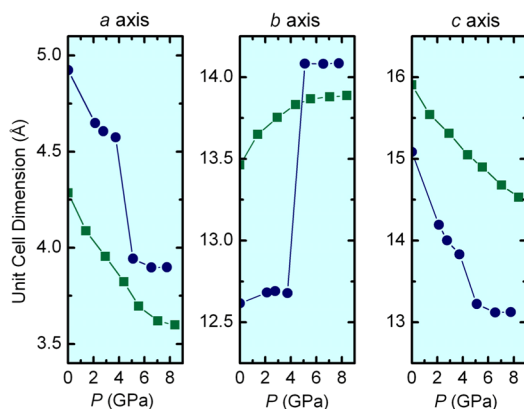


Figure 4. Cell dimensions of [1a]₂ (solid circles) and [1b]₂ (solid squares) as a function of pressure.

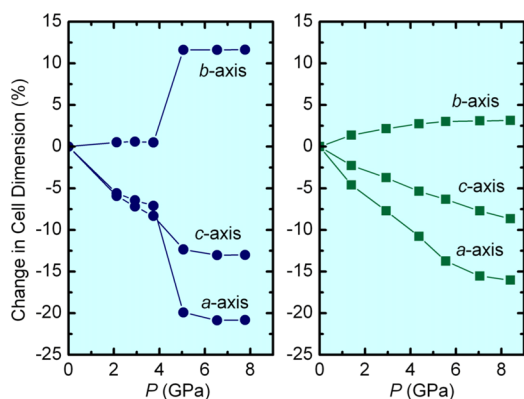


Figure 5. Relative changes in cell dimensions of [1a]₂ (left) and [1b]₂ (right) with increasing pressure.

coupled with the coarseness of the rigid body structural refinement, preclude a detailed interpretation of individual interactions, but it is instructive to note the tightening of the

coordination geometry about the deselenide core in [1a]₂ as a result of the phase change. By contrast, the packing environment in [1b]₂ remains relatively unchanged across the entire pressure range.

Conductivity Measurements. In previous work we determined the room temperature conductivity of both [1a]₂ and [1b]₂ to be on the order of 10^{-6} S cm⁻¹ at ambient pressure. We also explored the variation in conductivity with pressure, by means of a cubic anvil press, and established that in both cases the conductivity could be increased by 5–6 orders of magnitude by the application of 5 GPa pressure. Variable temperature conductivity measurements on [1a]₂ indicated that the value of the thermal activation energy E_{act} was reduced to near 0.03 eV at 5 GPa. Using a Walker module, we were able to extend the pressure limit to 9 GPa and, thereby, secure information on the dependence of E_{act} on pressure over the range $T = 300$ – 360 K. The derived trends in E_{act} with increasing pressure obtained from the two techniques (Figure 8) are consistent with the closure of the band gap in the region of 4–5 GPa.²⁸ We have now carried out similar variable temperature measurements on [1b]₂ over the range 0–5 GPa, using a cubic anvil press, and these reveal a more uniform, less precipitous decrease in E_{act} which reaches a value of 0.1 eV near 5 GPa, the limit of the experiment (Figure 8). Extrapolation of the data to higher pressures suggests that loss of activation would require pressures well above 10 GPa.

Band Electronic Structures. As in the case of [1a]₂,²¹ the room temperature electronic structure of [1b]₂ has been probed as a function of pressure by a series of ab initio calculations with the VASP package. Using the experimental structures at various pressures as starting points, complete optimizations of both geometry and pressure were performed. Details of the calculated molecular and solid state geometries (in CIF format) for representative pressures are available in the Supporting Information. As illustrated in Figure 9, plots of the calculated cell parameters over the pressure range 0–13.7 GPa are in good agreement with those obtained experimentally,

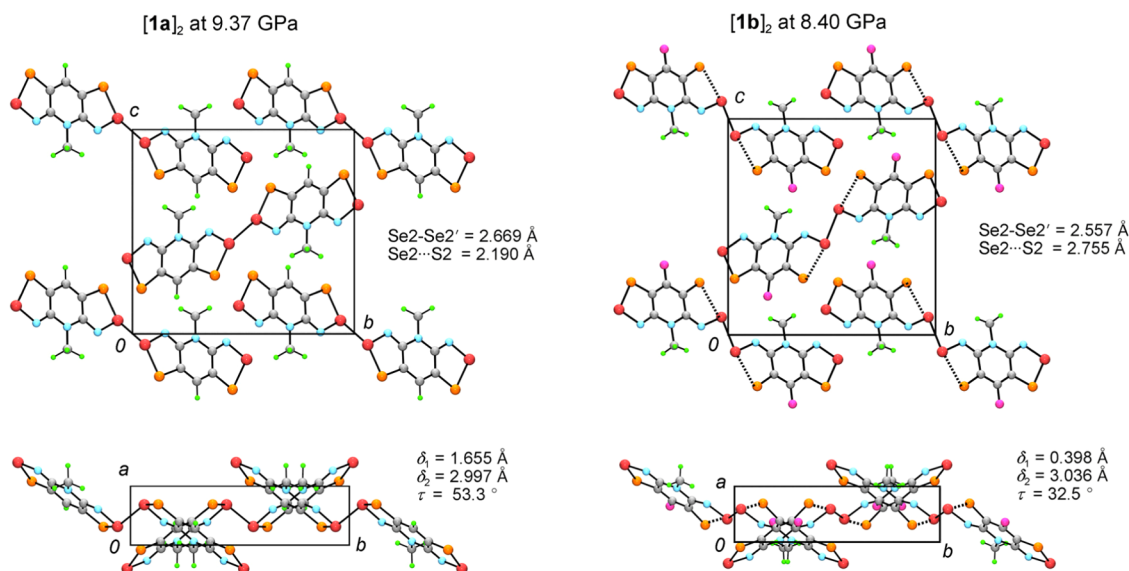


Figure 6. Unit cell drawings of $[1a]_2$ at 9.37 GPa (left) and $[1b]_2$ at 8.40 GPa (right), viewed along the a (above) and c (below) axes. See Figure 1 for definition of distances and angles.

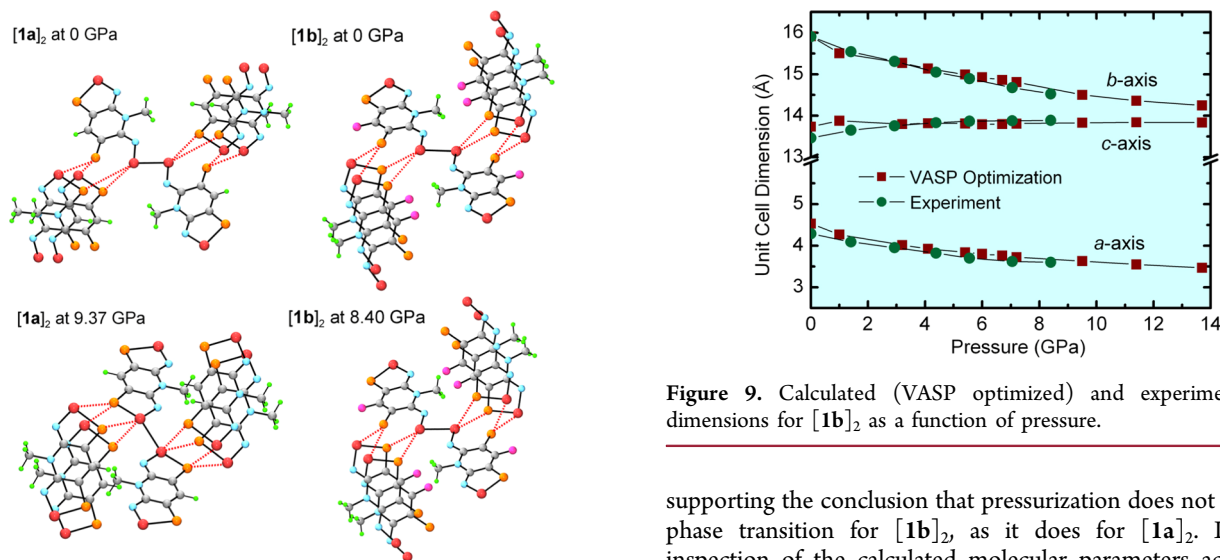


Figure 7. Coordination about the diselenide core in $[1a]_2$ and $[1b]_2$ as a function of pressure. The intermolecular contacts $Se2 \cdots S1'$ and $S2 \cdots Se1'$ (red dashed lines) are listed in Table 2.

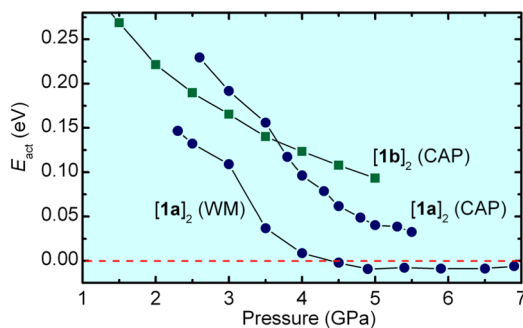


Figure 8. Pressure dependence of the activation energy E_{act} for conductivity of $[1a]_2$ and $[1b]_2$ over the range $T = 300\text{--}360$ K, as measured using a cubic anvil press (CAP) and a Walker module (WM). The data for $[1a]_2$ are from refs 17a and 21.

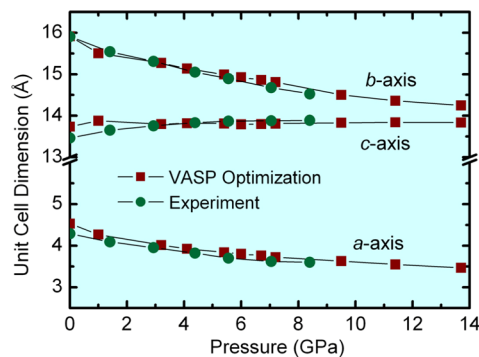


Figure 9. Calculated (VASP optimized) and experimental cell dimensions for $[1b]_2$ as a function of pressure.

supporting the conclusion that pressurization does not induce a phase transition for $[1b]_2$, as it does for $[1a]_2$. Likewise, inspection of the calculated molecular parameters across the entire pressure range provides no evidence of buckling of the dimer.

Based on the success of the VASP package in replicating the observed geometry of $[1b]_2$ as a function of pressure, we have examined its band electronic structure as a function of pressure, using the same computational method. The results are illustrated in Figure 10, in the form of crystal orbital dispersion diagrams at four well-separated pressures in the range 0–10 GPa. As may be seen, there is a well-defined energy gap E_g between the valence and conduction bands at ambient pressure, as expected for a closed shell semiconductor (for which $E_g \sim 2E_{act}$). With increasing pressure, the valence and conduction bands are broadened, as a result of increased intermolecular overlap, and there is a concomitant decrease in E_g , which reaches a value of 0.08 eV at 9.5 GPa. However, final coalescence of the valence and conduction bands does not take place until > 13 GPa.

In order to compare the behavior of $[1b]_2$ with that previously reported for $[1a]_2$, we provide in Figure 11 a comparison of the pressure dependence of the calculated band gap for the two compounds. The slow, steady decrease in E_g is

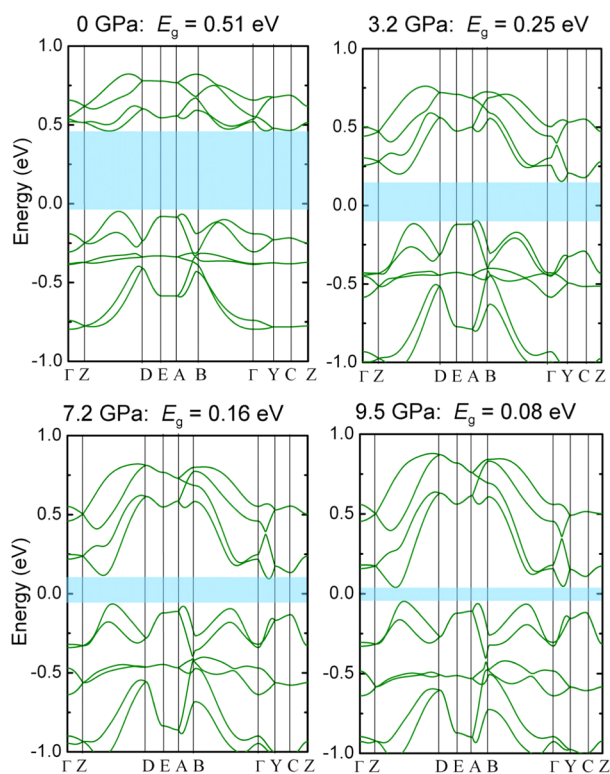


Figure 10. VASP band dispersion diagrams for $[1b]_2$, as a function of pressure. The hatched zone (in blue) denotes the indirect band gap E_g .

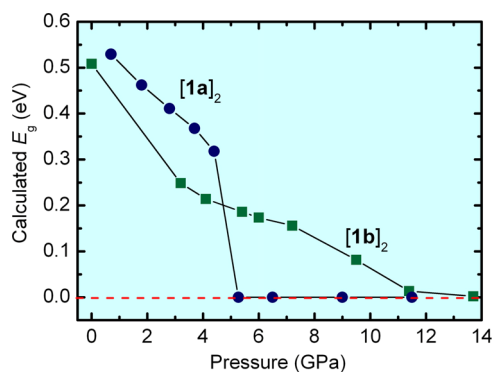


Figure 11. Band gaps E_g obtained from VASP optimized structures of $[1a]_2$ and $[1b]_2$ as a function of pressure. The data for $[1a]_2$ are from ref 21.

in marked contrast to that seen for $[1a]_2$, which undergoes a rapid drop in E_g in the region of the phase transition from σ -dimer to π -dimer.

DISCUSSION

In recent years there has been a surge in interest in the development of structure–property correlations for organic magnetic and conductive materials as a function of pressures at pressures below 10 GPa. The critical challenge is to establish whether the function of molecular materials under mild pressure can be understood and, hence, fine-tuned. The ability to pursue this goal has been driven in large part by the increasing availability of synchrotron radiation and diamond anvil techniques. These allow for a detailed mapping of the associated structural changes, which are often very subtle. Improvements in magnetic properties,²⁹ conductivity enhance-

ments,³⁰ and phase transitions associated with the coordination geometry³¹ have been effectively correlated with pressure-induced structural changes. In the present case the pair of dimers $[1a]_2$ and $[1b]_2$ provide a striking example of two isostructural molecular materials that display completely different responses to physical pressure. DFT calculations provide an impressive replication of the structural evolution and the associated changes in molecular and band electronic structures of the two compounds. The structural phase change observed for $[1a]_2$ near 5 GPa, which involves a buckling of the planar hypervalent $S\cdots Se-Se\cdots S$ unit and a closure of the molecular HOMO–LUMO gap, and hence the solid state band gap, is not found for $[1b]_2$. Instead, the latter material undergoes a more uniform compression, a process which involves virtually no change in molecular structure and causes only a gradual spreading of the valence and conduction bands. Band gap closure is not predicted to occur until $P > 13$ GPa.

What the computational results do not reveal, however, is why the pressure induced dichotomy exists at all. While we do not have a definitive answer to this question, a qualitative understanding of the issues can, we believe, be developed by comparing the two ambient pressure structures. As illustrated in Figure 12, the most notable difference between them at 0 GPa

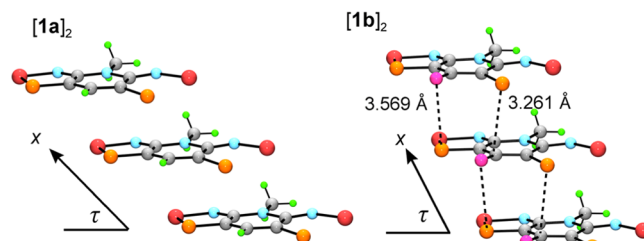


Figure 12. π -Stack slippage and interlayer contacts in $[1a]_2$ and $[1b]_2$ at ambient pressure.

is the degree of inclination of the mean planes of dimers with respect to the stacking direction, that is, the angle τ defined in Figure 1. In $[1a]_2$ τ is much larger (46.0°) than that in $[1b]_2$ (35.9°). Given that the two molecules differ only in the replacement of the basal proton in $[1a]_2$ with a fluorine atom in $[1b]_2$, this significant change in π -stack slippage is at first surprising, since their van der Waals radii ($r_H = 1.20$ Å, $r_F = 1.47$ Å) are comparable.²⁶ However, close inspection of the overlay of adjacent dimers along the π -stacks leads to the conclusion that the difference in π -stack inclination is not a steric issue, but rather one associated with the electronegativity of fluorine, which (i) leads to potential electrostatic interactions within the π -stacks and (ii) allows for the development of structure-strengthening $F\cdots H_3C$ contacts that influence the interlocking of neighboring π -stacks.

The first of these two effects is explored in Figure 13, which compares the charge density distribution in the heterocyclic core of $[1a]_2$ and $[1b]_2$, as calculated at the B3LYP/6-31G(d,p) level. As may be seen, there is a significant polarization of charge away from the C5 carbon in $[1b]_2$ (relative to $[1a]_2$) induced by the presence of the ligated fluorine. While this difference may not be the root cause of the reduced slippage of the π -stacks in $[1b]_2$, it is interesting to observe (Figure 12) that in this structure the C5 carbons are aligned almost perfectly on top of the negatively charged thione sulfurs S2, with $d(C5-S2) = 3.261$ Å. At the same time, on the other side of the molecule, there is a close interlayer contact (3.569 Å)

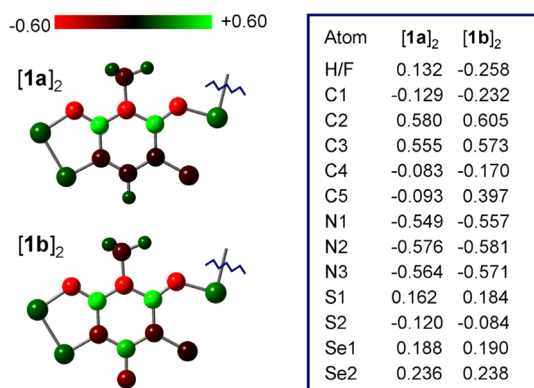


Figure 13. B3LYP/6-31G(d,p) charge distribution in [1a]₂ and [1b]₂ at ambient pressure.

between fluorine and the positively charged endocyclic sulfur S1.

The second issue noted above concerns the possibility that the close CH₃⋯F(aryl) contacts in [1b]₂ may be serving as supramolecular synthons³² which control the degree of slippage of the π -stacks. The potential for covalently bound fluorine atoms to enter into weak “hydrogen bridge” interactions is well-known in organic structures.^{33,34} Such donor/acceptor CH₃⋯F(aryl) contacts are strongest when the hybridization at the donor carbon is sp² or sp. When sp³ hybrids are involved, the hydrogen is less acidic, and CH₃⋯F(aryl) interactions are weaker still, but their influence can still be observed, as in the π -stacking of benzimidazolyl-nitronyl nitroxides.^{29b} Given these precedents, it is noteworthy that the more nearly superimposed stacking in [1b]₂ is associated with, if not actually induced by, two close CH₃⋯F(aryl) contacts (Figure 14).³⁵ By contrast, the

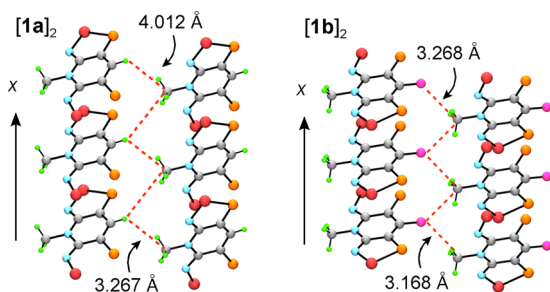


Figure 14. Interstack CH₃⋯H(aryl) and CH₃⋯F(aryl) contacts in [1a]₂ and [1b]₂ at ambient pressure (see ref 35).

increased slippage seen in [1a]₂ gives rise to only one short CH₃⋯H(aryl) approach. In the latter case, this feature may indeed be desirable, as these CH₃⋯H(aryl) interactions are likely repulsive.

The marked difference in the response of [1a]₂ and [1b]₂ to pressure prompts one final question. If it were possible to probe the compression of [1a]₂ in the absence of buckling, what would be the energy and electronic properties of the undistorted structure in the high pressure regime? To address this question, we performed a series of VASP calculations on [1a]₂ invoking gradual *isostructural compression* of the experimental ambient pressure structure. In this way, the phase change was effectively bypassed. Figure 15a compares the VASP unit cell volume V_{cell} of the two modifications of [1a]₂, that is the experimental π -dimer phase and a hypothetical σ -dimer phase derived using isostructural compression to

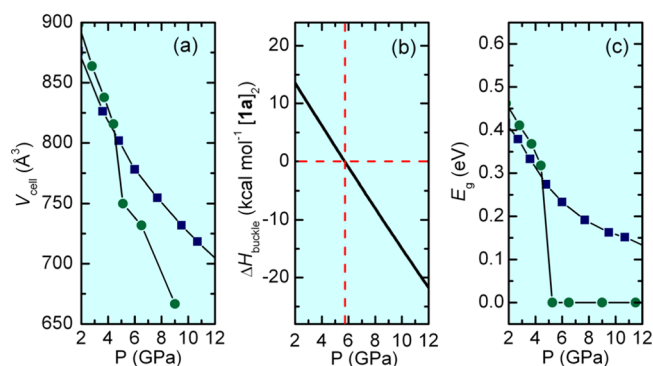


Figure 15. (a) Calculated cell volume V_{cell} of σ -dimer and π -dimer phases of [1a]₂ as a function of pressure. (b) Calculated enthalpy difference ΔH_{buckle} for the σ -dimer to π -dimer phase conversion of [1a]₂ as a function of pressure. (c) Calculated band gap E_g of the σ -dimer and π -dimer phases of [1a]₂ as a function of pressure. In parts a and c, data for the σ -dimer and π -dimer phases are represented respectively by blue squares and green circles.

suppress the phase transition. It is readily apparent that the hypothetical σ -dimer form undergoes a steady compression across the entire pressure range examined (0–14 GPa), but with formation of a π -dimer there is a contraction near 5 GPa. The enthalpy H of each phase as a function of pressure was estimated from the identity expression $H = E + PV$, using the total electronic energy E from the VASP calculations. The difference between the enthalpy values derived for each phase, that is the enthalpy change ΔH_{buckle} for the buckling process, is plotted in Figure 15b. As expected, the uniformly compressed (σ -dimer) structure is predicted to be more stable at low pressures, with the buckled π -dimer taking over at higher pressures. Given the size of the computational problem, the predicted transition pressure of 5.7 GPa (the vertical line in Figure 15b) is in remarkably good agreement with experiment. Finally, Figure 15(c) provides a visual comparison of the indirect band gap E_g of the buckled and unbuckled forms as a function of pressure. Perhaps not surprisingly, the results for the σ -dimer modification of [1a]₂ are reminiscent of those illustrated in Figure 11 for [1b]₂. Essentially, without buckling, the band gap of [1a]₂ is predicted not to occur until well above 14 GPa.

SUMMARY AND CONCLUSIONS

Predicting or even modifying the crystal structures of molecular solids is never easy, as changes in molecular structure can often have a significant effect on crystal structure.³⁶ The rich variety of space groups observed for bis-thiaselenazolyl radicals **1** with different R₁/R₂ groups²³ provides a clear demonstration of how relatively minor molecular tinkering can induce completely different crystal packing patterns and, hence, alter physical and electronic properties. Examples of **1** that dimerize are few, but when solid state association does occur, as in [1a]₂ and [1b]₂, the two radicals are linked via hypervalent 4c–6e S⋯Se–Se⋯S interactions. The resulting σ -dimers are isostructural at ambient pressure, crystallizing in the monoclinic space group $P2_1/c$ and packing in cross-braced slipped π -stacked arrays. Pairing of the spins affords a diamagnetic ground state, and both materials behave as small band gap semiconductors.

The significance of the present work lies in the fact that it demonstrates that the similarity in the structure and transport properties of [1a]₂ and [1b]₂ breaks down with the application

of pressure. Dimer $[1a]_2$ undergoes a phase transition near 5 GPa in which the unit cell experiences a “pancake-like” collapse, and the σ -dimer molecular structure buckles into a distorted π -dimer. By contrast, the unit cell of $[1b]_2$ undergoes a relatively uniform compression, with no change in the structure of the molecular dimer. Variable pressure conductivity measurements demonstrate that the phase transition in $[1a]_2$ gives rise to a metallic state, while compression of $[1b]_2$ produces a much more gradual closure of the band gap, with metallization not anticipated until > 13 GPa. The experimental results are supported by detailed VASP calculations on both $[1a]_2$ and $[1b]_2$, which predict the pressure required for the phase transition with impressive accuracy. Taken as a whole, the differing response of the structures of $[1a]_2$ and $[1b]_2$ to applied pressure emphasizes the need for detailed structural studies in order to understand and correlate the physical properties of molecular materials under pressure.

■ EXPERIMENTAL AND COMPUTATIONAL METHODS

Sample Preparation. Microcrystalline samples of $[1b]_2$ suitable for powder diffraction work were generated by reduction of the salt $[1b][OTf]$ (OTf = trifluoromethanesulfonate) with decamethylferrocene. Details of the procedure, and the preparation of $[1b][OTf]$, are described elsewhere.²³

Crystallography. High pressure, ambient temperature diffraction experiments on $[1b]_2$ were performed at BLX10U, SPring-8, using synchrotron radiation ($\lambda = 0.51446$ Å) and a powdered sample mounted in a diamond anvil cell, with helium as the pressure transmitting medium. The diffraction data were collected at room temperature and as a function of increasing pressure. A total of nine data sets from 0 to 11.21 GPa were indexed and the cell parameters refined using DASH 3.1.³⁷ Six of these data sets were solved in DASH starting from a model half-dimer based on the atomic coordinates of **1a** with the H-substituent replaced by a fluorine atom (with $d(C-F) = 1.30$ Å). During the Rietveld³⁸ refinement in DASH, a rigid-body constraint was maintained.³⁹ At this point, the space group settings were adjusted so as to allow a direct comparison of all the cell parameters with those published for $[1a]_2$. For three data sets (Table 1), the settings and atomic coordinates from the DASH solution were then taken into GSAS⁴⁰ for a final Rietveld refinement. Data from $2\theta = 3-20^\circ$ were refined with fixed atomic positions and isotropic thermal parameters with an assigned value of 0.025.

High Pressure Conductivity Measurements. High pressure conductivity experiments on $[1a,b]_2$ were carried out in a cubic anvil press⁴¹ using pyrophyllite ($Al_2Si_4O_{10}(OH)_2$) as the pressure transmitting medium. Sample pressure was determined from previous calibrations of the applied hydraulic load against pressures of structure transformations in standards at room temperature ($Hg \text{ I} \leftarrow \text{II}$ at 0.75 GPa, $Bi \text{ I} \leftarrow \text{II}$ at 2.46 GPa, $Tl \text{ I} \leftarrow \text{III}$ at 3.70 GPa, and $Ba \text{ I} \leftarrow \text{II}$ at 5.5 GPa).⁴² Two Pt electrodes contacted the precompacted, powder samples which were contained in a boron nitride ($\sigma_{BN} \approx 10^{-11} \text{ S cm}^{-1}$) cup. Four-wire AC (Solartron 1260 Impedance Analyzer) resistance measurements were made at a frequency of 1 kHz. The contiguous disk-shaped sample was extracted from the recovered pressure cell, and the sample geometry was measured to convert resistance to conductivity.

Electronic Structure Calculations. Charge densities for $[1a]_2$ and $[1b]_2$ were calculated using the UB3LYP functional and the split-valence double- ζ basis set 6-31G(d,p), as contained in the Gaussian 09W suite of programs.⁴³ Full geometry optimization was invoked. All solid state electronic structure calculations were performed with the electronic code VASP (Vienna Ab initio Structure Package)⁴⁴ employing projector augmented wave potentials⁴⁵ (PAW) to replace the core orbitals of all elements except H. The Perdew–Burke–Ernzerhof exchange and correlation functionals⁴⁶ within the generalized gradient approximation were used. The wave functions

were expanded in plane wave basis sets. A grid of $4 \times 2 \times 2$ k -points was used in the SCF and geometry optimization calculations. A more dense $16 \times 4 \times 4$ k -point set was used for the calculation of the electron density of states. For $[1b]_2$ the crystal geometry at different pressures was used as starting point for geometry optimizations. In order to generate the equation of state for the hypothetical σ -dimer variant of $[1a]_2$, isostructural compression of the ambient pressure crystal geometry was invoked. For the π -dimer form, the observed crystal geometry at different pressures was used as a starting point for geometry optimization. This process afforded two separate equations of state, from which the enthalpy ($H = E + PV$) of the σ - and π -dimers was evaluated as a function of pressure. The difference ΔH_{buckle} is plotted in Figure 15b. The reason for performing two set of calculations even though there is no change in the crystal symmetry is that the theoretical calculations were performed at 0 K, and spontaneous transformation from the σ - to π -dimer is not expected, as there is no thermal activation.

■ ASSOCIATED CONTENT

Supporting Information

Details of DFT and VASP calculations of $[1a]_2$ and $[1b]_2$ as a function of pressure; details of crystallographic data collection and structure refinement, tables of atomic coordinates, bond distances and angles, and isotropic thermal parameters in CIF format. This material is available free of charge via the Internet at <http://pubs.acs.org>.

■ AUTHOR INFORMATION

Corresponding Author

*E-mail address: oakley@uwaterloo.ca.

Notes

The authors declare no competing financial interest.

■ ACKNOWLEDGMENTS

We thank the Natural Sciences and Engineering Research Council of Canada (NSERCC) for financial support. We also thank the NSERCC for a Vanier Graduate Scholarship to K.L. and a Canada Graduate Scholarship to A.A.L., the Government of Canada for a Tier I Canada Research Chair to J.S.T., and the Japan Synchrotron Radiation Research Institute (JASRI) for beam time.

■ REFERENCES

- (1) (a) Grochala, W.; Hoffmann, R.; Feng, J.; Ashcroft, N. W. *Angew. Chem., Int. Ed.* **2007**, *46*, 3620. (b) MacMillan, P. F. *Chem. Soc. Rev.* **2006**, *35*, 855. (c) Hemley, R. J. *Annu. Rev. Phys. Chem.* **2000**, *51*, 763.
- (2) Riggelman, B. M.; Drickamer, H. G. *J. Chem. Phys.* **1963**, *38*, 2721.
- (3) (a) Takemura, K.; Minomura, S.; Shimomura, O.; Fujii, Y.; Axe, J. D. *Phys. Rev. B* **1982**, *26*, 998. (b) Kenichi, K.; Kyoko, S.; Hiroshi, F.; Mitsuko, O. *Nature* **2003**, *423*, 971.
- (4) (a) Akahama, Y.; Kobayashi, M.; Kawamura, H. *Phys. Rev. B* **1993**, *48*, 6862. (b) Luo, H.; Greene, R. G.; Ruoff, A. L. *Phys. Rev. Lett.* **1993**, *71*, 2943. (c) Akahama, Y.; Kobayashi, M.; Kawamura, H. *Phys. Rev. B* **1993**, *47*, 20.
- (5) Crapanzano, L.; Crichton, W. A.; Monaco, G.; Bellissent, R.; Meouar, M. *Nat. Mater.* **2005**, *4*, 550.
- (6) Cherin, P.; Unger, P. *Inorg. Chem.* **1967**, *6*, 1589.
- (7) Miyamoto, Y. *Jpn. J. Appl. Phys.* **1980**, *19*, 1813.
- (8) Brillante, A.; Della Valle, R. G.; Farina, L.; Venutti, E.; Cavazzoni, C.; Emerson, A. P. J.; Syassen, K. *J. Am. Chem. Soc.* **2005**, *127*, 3038.
- (9) (a) Nakayama, A.; Aoki, K.; Carlón, R. P. *Phys. Rev. B: Condens. Matter* **2001**, *64*, 064104. (b) Nakayama, A.; Fujihisa, H.; Takemura, K.; Aoki, K.; Carlón, R. P. *Synth. Met.* **2001**, *120*, 767. (c) Iwasaki, E.; Shimizu, K.; Amaya, K.; Nakayama, A.; Aoki, K.; Carlón, R. P. *Synth. Met.* **2001**, *120*, 1003.

- (10) (a) Nakayama, A.; Fujihisa, H.; Aoki, K.; Shirotani, I. *Synth. Met.* **1999**, *103*, 1901. (b) Nakayama, A.; Aoki, K.; Matsushita, Y.; Shirotani, I. *Solid State Commun.* **1999**, *110*, 627. (c) Shirotani, I.; Hayashi, J.; Yakushi, K.; Takeda, K.; Yokota, T.; Shimizu, K.; Amaya, K.; Nakayama, A.; Aoki, K. *Physica B* **2001**, *304*, 6.
- (11) Takemura, K.; Minomura, S.; Shimomura, O.; Fujii, Y. *Phys. Rev. Lett.* **1980**, *45*, 1881.
- (12) Tateyama, Y.; Ohno, T. *J. Phys.: Condens. Matter* **2002**, *14*, 10429.
- (13) Cui, H.; Brooks, J. S.; Kobayashi, A.; Kobayashi, H. *J. Am. Chem. Soc.* **2009**, *131*, 6358.
- (14) (a) Shirotani, I.; Kamura, Y.; Inokuchi, H.; Hirooka, T. *Chem. Phys. Lett.* **1976**, *40*, 257. (b) Onodera, A.; Shirotani, I.; Inokuchi, H.; Kawai, N. *Chem. Phys. Lett.* **1974**, *25*, 296.
- (15) Cui, H.; Okano, Y.; Zhou, B.; Kobayashi, A.; Kobayashi, H. *J. Am. Chem. Soc.* **2008**, *130*, 3738.
- (16) Tulip, P. R.; Bates, S. P. *J. Phys. Chem. C* **2009**, *113*, 19310.
- (17) (a) Beer, L.; Brusso, J. L.; Haddon, R. C.; Itkis, M. E.; Kleinke, H.; Leitch, A. A.; Oakley, R. T.; Reed, R. W.; Richardson, J. F.; Secco, R. A.; Yu, X. *J. Am. Chem. Soc.* **2005**, *127*, 1815. (b) Beer, L.; Brusso, J. L.; Haddon, R. C.; Itkis, M. E.; Leitch, A. A.; Oakley, R. T.; Reed, R. W.; Richardson, J. F. *Chem. Commun.* **2005**, 1543.
- (18) Hypervalent 4c–6e bonds involving combinations of S, Se, and/or Te are well-known for systems in which the terminal chalcogens are saturated. See, for example: (a) Nakanishi, W.; Hayashi, S.; Toyota, S. *Chem. Commun.* **1996**, 371. (b) Nakanishi, W.; Hayashi, S.; Arai, T. *Chem. Commun.* **2002**, 2416. (c) Nakanishi, W.; Hayashi, S.; Morinaka, S.; Sasamori, T.; Tokitoh, N. *New J. Chem.* **2008**, *32*, 1881. (d) Sharma, S.; Selvakumar, K.; Singh, V. P.; Zade, S. S.; Singh, H. B. *Phosphorus, Sulfur Silicon Relat. Elem.* **2008**, *183*, 827.
- (19) (a) Oakley, R. T.; Reed, R. W.; Cordes, A. W.; Craig, S. L.; Graham, S. B. *J. Am. Chem. Soc.* **1987**, *109*, 7745. (b) Del Bel Belluz, P.; Cordes, A. W.; Kristof, E. M.; Kristof, P. W.; Liblong, S. W.; Oakley, R. T. *J. Am. Chem. Soc.* **1989**, *111*, 9276. (c) Cordes, A. W.; Haddon, R. C.; Oakley, R. T.; Schneemeyer, L. F.; Waszczak, J. V.; Young, K. M.; Zimmerman, N. M. *J. Am. Chem. Soc.* **1991**, *113*, 582. (d) Parvez, M.; Boeré, R. T. *Acta Crystallogr., C* **1995**, *51*, 2118. (e) Wu, J.; MacDonald, D. J.; Clérac, R.; Jeon, I.; Jennings, M.; Lough, A. J.; Britten, J.; Robertson, C.; Dube, P. A.; Preuss, K. E. *Inorg. Chem.* **2012**, *51*, 3827.
- (20) Other, less symmetric modes of association, have also been observed. See, for example: (a) Bestari, K.; Cordes, A. W.; Oakley, R. T.; Young, K. M. *J. Am. Chem. Soc.* **1990**, *112*, 2249. (b) Feeder, N.; Less, R. J.; Rawson, J. M.; Olliet, P.; Palacio, F. *Chem. Commun.* **2000**, 2449.
- (21) Tse, J. S.; Leitch, A. A.; Yu, X.; Bao, X.; Zhang, S.; Liu, Q.; Jin, C.; Secco, R. A.; Desgreniers, S.; Ohishi, Y.; Oakley, R. T. *J. Am. Chem. Soc.* **2010**, *132*, 4876.
- (22) Selenium enters a metallic state near 25 GPa. (a) Riggelman, B. M.; Drickamer, H. G. *J. Chem. Phys.* **1962**, *37*, 446. (b) Bundy, F. P.; Dunn, K. J. *J. Chem. Phys.* **1979**, *71*, 1550.
- (23) Leitch, A. A.; Yu, X.; Robertson, C. M.; Secco, R. A.; Tse, J. S.; Oakley, R. T. *Inorg. Chem.* **2009**, *48*, 9874.
- (24) The structural results for [1b]₂ at 0 GPa reported here supersede those reported in ref 23, as the synchrotron diffraction data is of superior quality.
- (25) Chen, C. M.; Dojahn, J. G.; Wentworth, W. E. *J. Phys. Chem. A* **1997**, *101*, 3088.
- (26) (a) Bondi, A. *J. Phys. Chem.* **1964**, *68*, 441. (b) Dance, I. *New J. Chem.* **2003**, *27*, 22.
- (27) The structural details of the ambient pressure structure of [1a]₂ are based on the refinement of single crystal data.
- (28) The E_{act} values from the Walker module experiments are shifted to lower pressure compared with the cubic anvil values. This may result from the differences in pressure calibration in the two devices as well as the differences in hydrostaticity of the pressure medium used in each device (pyrophyllite versus MgO).
- (29) (a) Mito, M.; Komorida, Y.; Tsuruda, H.; Tse, J. S.; Desgreniers, S.; Ohishi, Y.; Leitch, A. A.; Cvrkalj, K.; Robertson, C. M.; Oakley, R. T. *J. Am. Chem. Soc.* **2009**, *131*, 16012. (b) Seber, G.; Halder, G. J.; Schlueter, J. A.; Lahti, P. M. *Cryst. Growth Des.* **2011**, *11*, 4261. (c) Thomson, R. I.; Pask, C. M.; Lloyd, G. O.; Mito, M.; Rawson, J. M. *Chem. Eur. J.* **2012**, *18*, 8629. (d) Schlueter, J. A.; Park, H.; Halder, G. J.; Armand, W. R.; Dunmars, C.; Chapman, K. W.; Manson, J. L.; Singleton, J.; McDonald, R.; Plonczak, A.; Kang, J.; Lee, C.; Whangbo, M.-H.; Lancaster, T.; Steele, A. J.; Franke, I.; Wright, J. D.; Blundell, S. J.; Pratt, F. L.; de George, J.; Turnbull, M. M.; Landee, C. P. *Inorg. Chem.* **2012**, *51*, 2121.
- (30) Leitch, A. A.; Lekin, K.; Winter, S. M.; Downie, L. E.; Tsuruda, H.; Tse, J. S.; Mito, M.; Desgreniers, S.; Dube, P. A.; Zhang, S.; Liu, Q.; Jin, C.; Ohishi, Y.; Oakley, R. T. *J. Am. Chem. Soc.* **2011**, *133*, 605.
- (31) (a) Halder, G. J.; Chapman, K. W.; Schlueter, J. A.; Manson, J. L. *Angew. Chem., Int. Ed.* **2011**, *50*, 419. (b) Prescimone, A.; Morien, C.; Allan, D.; Schlueter, J. A.; Tozer, S. W.; Manson, J. L.; Parsons, S.; Brechin, E. K.; Hill, S. *Angew. Chem., Int. Ed.* **2012**, *51*, 7490.
- (32) Desiraju, G. R. *Angew. Chem., Int. Ed.* **1995**, *34*, 2311.
- (33) (a) Desiraju, D. G. *Acc. Chem. Res.* **2002**, *35*, 565. (b) Thakur, T. S.; Kirchner, M. T.; Bläser, D.; Boese, R.; Desiraju, D. R. *CrystEngComm* **2010**, *12*, 2079.
- (34) (a) Weiss, H.-C.; Boese, R.; Smith, H. L.; Haley, M. M. *Chem. Commun.* **1997**, 2403. (b) Thalladi, V. R.; Weiss, H. C.; Bläser, D.; Boese, R.; Nangia, A.; Desiraju, D. R. *J. Am. Chem. Soc.* **1998**, *120*, 8702. (c) Mele, A.; Vergani, B.; Viani, F.; Meille, S. V.; Farina, A.; Bravo, F. *Eur. J. Org. Chem.* **1999**, 187. (d) Haufe, G.; Rosen, T. C.; Meyer, O. G. J.; Fröhlich, R.; Rissanen, K. *J. Fluorine Chem.* **2002**, *114*, 189. (e) Hyla-Kryspin, E.; Haufe, G.; Grimme, S. *Chem. Eur. J.* **2004**, *10*, 3411.
- (35) The contacts shown and distances specified in Figure 14 are from the aryl proton to the methyl carbon, as the positions of the methyl protons (which are free to rotate) are arbitrary.
- (36) “One of the fundamental problems, however, remains unsolvable: the prediction of the crystal structure of organic molecules and the planned assembly of structures with predetermined properties is possible only within modest limits.” Enkelmann, V. *Angew. Chem., Int. Ed.* **1991**, *30*, 1121.
- (37) David, W. I. F.; Shankland, K.; van de Streek, J.; Pidcock, E.; Motherwell, W. D. S.; Cole, J. C. *J. Appl. Crystallogr.* **2006**, *39*, 910.
- (38) Rietveld, H. M. *J. Appl. Crystallogr.* **1969**, *2*, 65.
- (39) As a result of the rigid body refinement model, standard deviations are not given for the bond and angle metrics for [1a]₂ or [1b]₂ obtained from powder diffraction data.
- (40) Larson, A. C.; Von Dreele, R. B. Report No. LA-UR-86-748; Los Alamos National Laboratory: Los Alamos, NM, 1987.
- (41) Secco, R. A. *Can. J. Phys.* **1995**, *73*, 287.
- (42) Secco, R. A.; Schloessin, H. H. *J. Appl. Phys.* **1986**, *60*, 1625.
- (43) Frisch, M. J.; Trucks, G. W.; Schlegel, H. B.; Scuseria, G. E.; Robb, M. A.; Cheeseman, J. R.; Scalmani, G.; Barone, V.; Mennucci, B.; Petersson, G. A.; Nakatsuji, H.; Caricato, M.; Li, X.; Hratchian, H. P.; Izmaylov, A. F.; Bloino, J.; Zheng, G.; Sonnenberg, J. L.; Hada, M.; Ehara, M.; Toyota, K.; Fukuda, R.; Hasegawa, J.; Ishida, M.; Nakajima, T.; Honda, Y.; Kitao, O.; Nakai, H.; Vreven, T.; Montgomery, J. A., Jr.; Peralta, J. E.; Ogliaro, F.; Bearpark, M.; Heyd, J. J.; Brothers, E.; Kudin, K. N.; Staroverov, V. N.; Kobayashi, R.; Normand, J.; Raghavachari, K.; Rendell, A.; Burant, J. C.; Iyengar, S. S.; Tomasi, J.; Cossi, M.; Rega, N.; Millam, N. J.; Klene, M.; Knox, J. E.; Cross, J. B.; Bakken, V.; Adamo, C.; Jaramillo, J.; Gomperts, R.; Stratmann, R. E.; Yazyev, O.; Austin, A. J.; Cammi, R.; Pomelli, C.; Ochterski, J. W.; Martin, R. W.; Morokuma, K.; Zakrzewski, V. G.; Voth, G. A.; Salvador, P.; Dannenberg, J. J.; Dapprich, S.; Daniels, A. D.; Farkas, O.; Foresman, J. B.; Ortiz, J. V.; Cioslowski, J.; Fox, D. J. *Gaussian 09*, Revision A.02; Gaussian, Inc.: Wallingford, CT, 2009.
- (44) (a) Kresse, G.; Hafner, J. *Phys. Rev.* **1993**, *47B*, 558. (b) Kresse, G.; Furthmüller, J. *Phys. Rev.* **1996**, *54B*, 11169.
- (45) (a) Blöchl, P. E. *Phys. Rev.* **1994**, *50B*, 17953. (b) Kresse, G.; Joubert, J. *Phys. Rev.* **1999**, *59B*, 1758.
- (46) Perdew, J. P.; Burke, K.; Ernzerhof, M. *Phys. Rev. Lett.* **1996**, *77*, 3865.